J Mater Sci (2007) 42:6267–6273
DOI 10.1007/s10853-006-1252-8

Grain boundary analysis and secondary phases in $LaCoO_3$-based perovskites

Per Erik Vullum · Antonius T. J. van Helvoort · Randi Holmestad · Johann Mastin · Øystein E. Andersen · Mari-Ann Einarsrud · Tor Grande

Received: 11 July 2006 / Accepted: 10 November 2006 / Published online: 21 April 2007

Abstract Secondary phases and grain boundaries in $LaCoO_3$ and $La_{0.7}Sr_{0.3}CoO_{3-\delta}$ ceramics have been studied by transmission electron microscopy. Both materials contained small amounts of grains of a secondary phase; the face centered cubic spinel structure Co_3O_4, located at triple junctions. These grains were agglomerates of several smaller grains. High resolution electron microscopy combined with annular dark field scanning transmission electron microscopy and electron energy loss spectroscopy were used to analyze the grain boundaries. In $LaCoO_3$, the grain boundaries were sharp with stable compositions of La, Co and O across the boundaries. In $La_{0.7}Sr_{0.3}CoO_{3-\delta}$, a 1–2 nm thick intergranular layer between the grains was observed. This layer was rich in O and Co and deficient in Sr and La, compared to the nominal composition of the material.

Introduction

The nature of grain boundaries is of great importance with respect to the functional and structural properties in polycrystalline ceramic materials. This has been observed in a wide range of materials. In high temperature $YBa_2Cu_3O_{7-\delta}$ superconductors, for example, the critical current density J_c, is suppressed at grain boundaries [1–3]. By overdoping the grain boundaries relative to the grains, by replacing yttrium with calcium, the grain boundary J_c can be enhanced which is proven important for commercial applications [4]. Other examples include thin intergranular glassy phases, which are detrimental to the mechanical strength of the high temperature materials SiC [5, 6] and Si_3N_4 ceramics [7–9].

The present $LaCoO_3$-based materials have the cubic perovskite structure with space group $Pm\bar{3}m$ at high temperatures. By cooling, the materials undergo a second order, displacive phase transition, and they are rhombohedrally distorted with space group $R\bar{3}c$ at ambient temperature [10–12]. This second order improper paraelastic to ferroelastic phase transition is characterized by a G_{25} phonon soft mode collapse at the R-point (1/2, 1/2, 1/2) of the cubic lattice, and doubles the periodicity along the threefold axis, which becomes the unique axis of the rhombohedral ferroelastic state. Due to the mixed conductivity of the materials at elevated temperatures, they have potential applications for use as dense ceramic materials for oxygen separation from air and for syn gas production by partial oxidation of natural gas [13]. In addition, they are candidates as cathodes for solid oxide fuel cells and as catalysts [13]. The presence of secondary phases and/or grain boundaries with chemistry different than that of the bulk material may have significant influence for example on the transport and mechanical properties.

Transmission electron microscopy (TEM) is a versatile tool to gain information about grain boundary structures and chemistry of ceramics. High resolution transmission

P. E. Vullum (✉) · A. T. J. van Helvoort · R. Holmestad
Department of Physics, Norwegian University of Science and Technology, 7491 Trondheim, Norway
e-mail: per.vullum@phys.ntnu.no

J. Mastin · Ø. E. Andersen · M.-A. Einarsrud · T. Grande
Department of Materials Science and Engineering, Norwegian University of Science and Technology, 7491 Trondheim, Norway

electron microscopy (HRTEM) is a coherent imaging technique [14] where directly transmitted and diffracted beams interfere to form a phase contrast image in which the crystal lattice can be resolved with a high spatial resolution. The disadvantages of HRTEM are contrast reversals due to defocus and thickness variations and no direct interpretable discrimination between different elements. High angle annular dark field scanning TEM (HAADF STEM) imaging, on the other hand, is an incoherent imaging technique. The image is an amplitude image where the signal is dominated by incoherent thermal diffuse scattering [15–17], and contributions from Bragg diffraction and phase contrast vanish as the scatting angle increases. The intensity of the high angle scattered electrons increases with the atomic number, Z. This strong Z dependence makes the HAADF images sensitive to heavy elements, such as La and Sr. When HRTEM and HAADF STEM are combined with electron energy loss spectroscopy (EELS) and/or electron dispersive spectroscopy (EDS), TEM becomes a powerful tool to study both structure and chemistry down to sub-nanometer level [18].

To our knowledge, no grain boundary analysis has been reported for $LaCoO_3$-based materials. However, for $La_{1-x}Sr_xCoO_{3-\delta}$ the stability field for a single-phase material has shown to be very narrow, with secondary phases forming for small deviations in nominal stoichiometry between the cations [19]. Here we use the combination of HRTEM, annular dark field (ADF) imaging, EELS and EDS to study secondary phases and grain boundaries in the two compositions $LaCoO_3$ (LC) and $La_{0.7}Sr_{0.3}CoO_{3-\delta}$ (LSC). Additional phases on grain boundaries and triple points are determined and the materials are compared.

Experimental procedures

Submicron (0.1–0.5 μm), stoichiometric LC and LSC powders were prepared by spray pyrolysis of metal nitrate solutions. To provide stoichiometric powders of LSC, ethylenediamine tetraacetic acid was used as complexing agent. A detailed overview of the synthesis will be given elsewhere by Ø.E. Andersen and coworkers. The raw powders were calcined in air for 2 h (LSC) or 24 h (LC) at 900 °C and further ball milled in ethanol for 24 h. Cylindrical samples were made by uniaxial pressing at 45–60 MPa followed by isostatic pressing at 200 MPa. Sintering was performed in air at 1200 °C for 6 h (LSC) or 20 h (LC). The densities of the materials were 96% (LSC) or 98% (LC) measured by the Archimedes method using isopropanol.

The TEM samples were prepared by mechanical grounding of 3 mm in diameter discs to a thickness of 100 μm, followed by dimpling and ion milling at liquid nitrogen temperature to avoid breakage and to reduce the extent of the amorphous layer on the sample surface formed during ion milling. To further reduce the thickness of the amorphous layer on the sample surface, ion milling for 90 min with a thinning angle of 6° and progressively decreasing acceleration voltage from 2.5 to 1 keV after foil penetration was performed. Prior to the TEM analysis, the TEM foils and holder were cleaned in a Fischione model 1020 plasma cleaner.

A JEOL 2010F STEM/TEM electron microscope (200 kV field emission gun, C_s = 1.0 mm) was used for the analysis. The microscope was equipped with an INCA 200 TEM EDS system, a post-column Gatan imaging filter (GIF), in addition to JEOL annular bright field (ABF) and ADF detectors. Secondary phase grains were analyzed by HRTEM, EDS, and EELS. Grain boundaries were analyzed by HRTEM, ADF imaging, and EELS spectrum imaging (SI). ADF images were recorded using the ADF detector with collection angles ranging from 18 to 172 mrad depending on the intermediate lens settings. The scanning electron probe was 0.2 nm in diameter. HAADF images were recorded with a detector collection range of 68–172 mrad. Low angle annular dark field (LAADF) imaging was recorded in an angle range of 18–48 mrad. EELS-SI was performed with a scanning electron probe of 0.5 nm in diameter and using the GIF. The step size in every spectrum image perpendicular to the grain boundaries was chosen to be 0.5 nm and software controlled drift compensation was used during acquisition. The beam convergence angle was 12 mrad and the spectrometer collection angle was 13.5 mrad. Two different electron energy loss regions were used in SI to optimize the peak to background statistics for all relevant peaks. The first range covered the spectrum from 450 to 960 eV, using a dispersion of 0.5 eV per channel. The second range covered the spectrum from 75 to 1100 eV, using 1.0 eV per channel. The content of O, Co, and La was calculated from the first energy range and the Sr content was calculated from the second energy range. Alle peaks were fitted by using Hartree Slater cross sections and power law background models. The energy resolution, based on the zero loss peak, was between 0.9 and 1.0 eV.

Results and discussion

Secondary phases

The average grain sizes for the LC and LSC materials were about 5 and 2–3 μm, respectively. The overall oxygen non-stoichiometry was measured by thermogravimetry, as described elsewhere [20]. In LC the oxygen deficiency was neglectable, while for LSC δ = 0.01 at ambient temperature.

Small amounts of a secondary phase were found in both materials. The secondary phase was located at triple junctions and agglomerated in grains of about 0.5–1 μm in diameter, as shown in Fig. 1. The secondary phase grains consist of smaller sub-grains with sizes in the range of 100–200 nm. The cubic rock salt structure CoO and the cubic spinel structure Co_3O_4 are the stable oxides in the cobalt oxide system [21, 22]. The two structures can be distinguished by electron diffraction. The larger unit cell of the spinel lattice compared to the rock salt lattice can be directly identified. The sub-grains in the triple junctions of LC and LSC were crystalline and both having the spinel structure of Co_3O_4. EDS and EELS analysis confirmed that the secondary phase consisted of Co and O, with a slightly larger amount of O than Co. A HRTEM image from a sub-grain in LSC is shown in Fig. 2 with a corresponding diffraction pattern. The presence of Co_3O_4 is due to deviation from nominal cation stoichiometry in the starting powder, resulting in Co excess. Sr substituted $LaCoO_3$ have been shown not to tolerate even very small offsets from the ideal perovskite stoichiometry without formation of secondary phases [19], and the observed secondary phase is not due to incomplete annealing. Also in $La_{0.5}Sr_{0.5}Fe_{1-x}Co_xO_{3-\delta}$, observations of secondary phase Co_3O_4 have been reported [23].

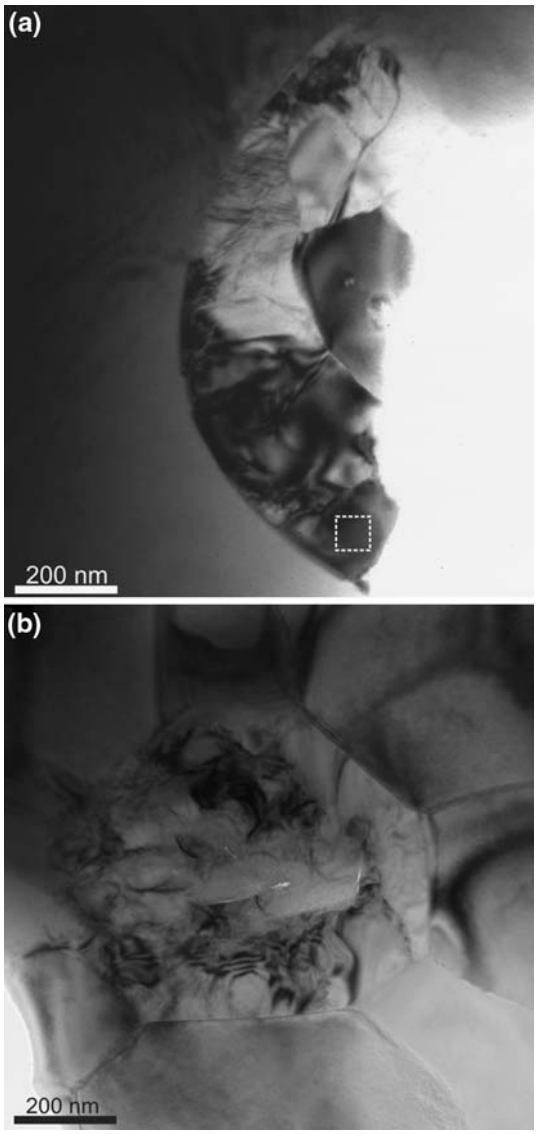

Fig. 1 Grains with Co_3O_4 in (**a**) LSC and (**b**) LC. The marked area in (**a**) corresponds to the magnified region in Fig. 2

Grain boundary analysis

In LC and LSC, the orientation relationships between the grains studied covered a wide range of angles. To analyze grain boundaries in the TEM, the boundary has to be parallel to the electron beam. If not thin layers with different chemistry than the nominal will be smeared out in the field of view due to the two-dimensional projection. Often the grain boundaries were found to be edge on if one of the grains was oriented in the pseudo cubic [100] or [110] zone axes. The grain on the other side of the boundary was then in an arbitrary orientation, away from any Bragg conditions. The orientation relationship between the grain boundaries therefore made electron diffraction combined with HRTEM an unsatisfactory technique to analyze the boundaries. However, ADF does not require on zone criteria and EELS should rather be performed off zone to avoid channeling effects [24].

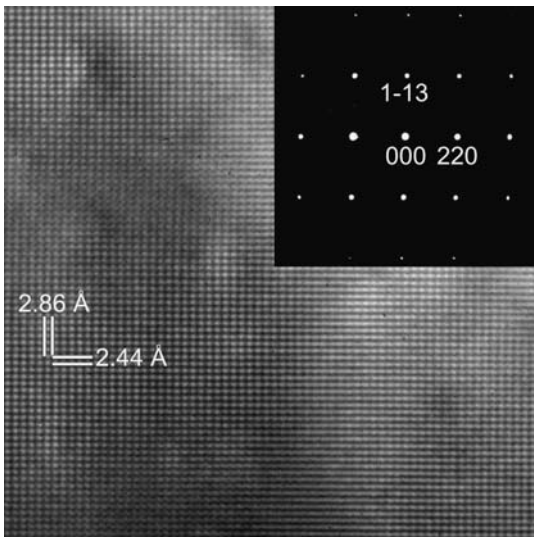

Fig. 2 High-resolution image of the cubic spinel structure of the Co_3O_4 secondary phase in LSC. The grain is oriented in the $[3\bar{3}\bar{2}]$ zone axis showing the (220) and $(\bar{1}\bar{1}3)$ planes in perpendicular directions. The inset shows the corresponding diffraction pattern

LC

A grain boundary with the upper grain oriented in the hexagonal [$\bar{1}$11] zone axis (corresponding to the pseudo cubic [110] zone axis) is shown in Fig. 3. The three images are (a) a HRTEM image, (b) a HAADF image, and (c) a LAADF image. The HRTEM image depicts a 2-nm thick layer along the grain boundary where the contrast is smeared out for the in-zone grain. There may be several explanations for this observed layer, such as a grain boundary layer with different chemistry and structure, strain contrast, or a boundary that is not completely parallel to the electron beam. However, ADF images from more than ten different grain boundaries all showed a sharp boundary with higher contrast for the in-zone grain compared to the darker out-of-zone grain. The LAADF image had a ~2 nm thick layer with higher intensity at the grain boundary. With increasing collection angle this layer became less visible and on the HAADF image, the contrast reversed with lower intensity of the grain boundary layer compared to the bulk intensity of the grain. The contrast reversal of the grain boundary layer between the LAADF and HAADF images is shown in Fig. 4. The intensity profiles in Fig. 4 also show the higher intensity on planes with La present since the heavy La atom scatters more and over larger angles than the smaller Co and O atoms.

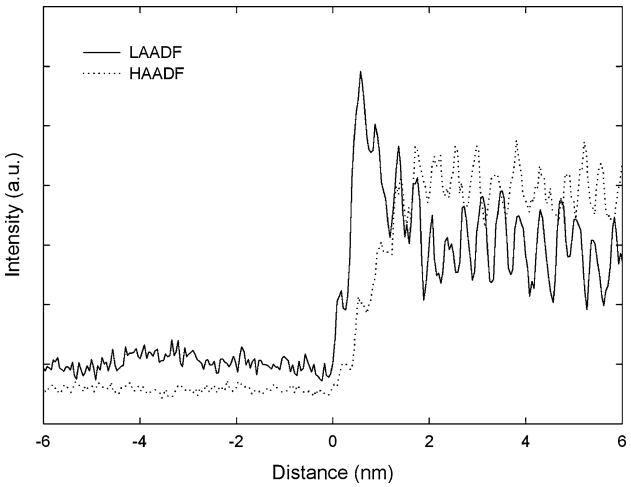

Fig. 4 The intensity profiles across the grain boundary for images (**b**) and (**c**) in Fig. 3. The grain boundary is located at 0 nm, with the in-zone grain above 0 nm and the out-of-zone grain below 0 nm. The profiles correspond to the rectangular dotted areas in Fig. 3(**b**) and (**c**). The peaks in the intensity profiles for the in-zone grain correspond to the La columns

Contrast reversal of the grain boundary layer between LAADF and HAADF indicates that the layer shows not purely *Z*-contrast. If there was a change in composition at the grain boundary, the layer should always be dark or

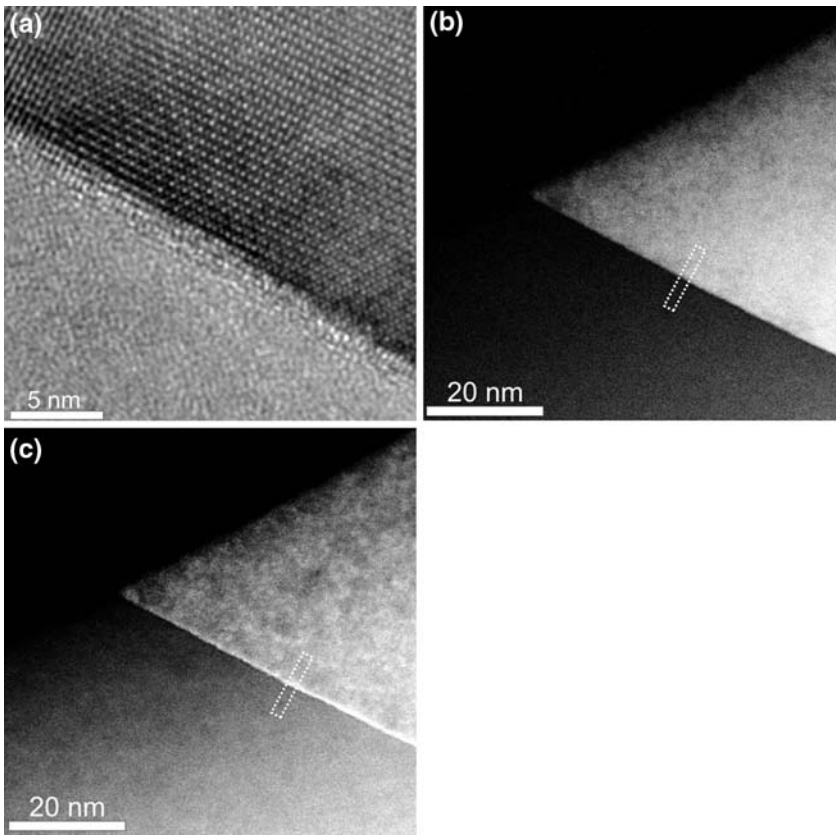

Fig. 3 A grain boundary in LC with the upper grain oriented in the hexagonal [$\bar{1}$11] zone axis (equal to the pseudo cubic [110] zone axis). (**a**) A bright field TEM image, (**b**) and (**c**) are HAADF and LAADF STEM images, respectively

bright, independent of collection angle. By tilting the upper grain slightly out-of-zone, the grain boundary layer disappeared. If the layer was due to *Z*-contrast, a small rotation of the sample should not make the contrast to vanish. However, when the layer is not edge on, the width of the layer should increase on the image with a corresponding loss of contrast. The origin of the grain boundary layer observed by ADF must therefore be due to some dechanneling effects. LAADF is more sensitive to contrast from dechanneling effects, such as strain contrast [25, 26] and phonon contrast [27, 28]. If the atomic columns in the grain boundary layer are not perfectly straight due to strain and/or a change of the phonon modes, some of the high angle scattered electrons scatter to lower angles. These electrons were then detected in the LAADF image instead of the HAADF image. Any of the two dechanneling effects can explain the enhanced signal at lower angles with a corresponding decrease of the signal at higher angles. To confirm the sharpness of the grain boundaries in LC, EELS-SI was performed across three different grain boundaries. All measurements showed a homogeneous distribution of the elements across the boundaries. Additionally, one grain boundary was studied by EDS. The EDS line scan indicated no variation of the chemical composition across the boundary.

LSC

ADF images, including more than ten different grain boundaries, all showed that the grain boundaries in LSC were different to those in LC. In Fig. 5, a grain boundary is imaged edge on with the upper grain oriented in the hexagonal [$\bar{4}\bar{2}1$] zone axis (equal to the pseudo cubic [001] zone axis). A grain boundary layer is indicated in the HRTEM image (Fig. 5(a)), but the image gives no information about the origin of the layer. A 1–2 nm thick layer with lower intensity at the grain boundary is shown in both the HAADF image (Fig. 5(b)) and the LAADF image (Fig. 5(c)). In the LAADF image a bright layer, equal to that observed in LC, is also evident adjacent to the dark, low intensity layer. The intensity profiles for the HAADF and LAADF images are shown in Fig. 6. The low intensity layer A and the dechanneling B layer are both evident. The layer with lower intensity at the grain boundary, independent of collection angle, indicates a different composition with less heavy elements in this layer compared to the bulk material. The dechanneling layer disappeared when the upper grain was tilted away from the zone axis. The low intensity layer was still present, however broadened with less contrast.

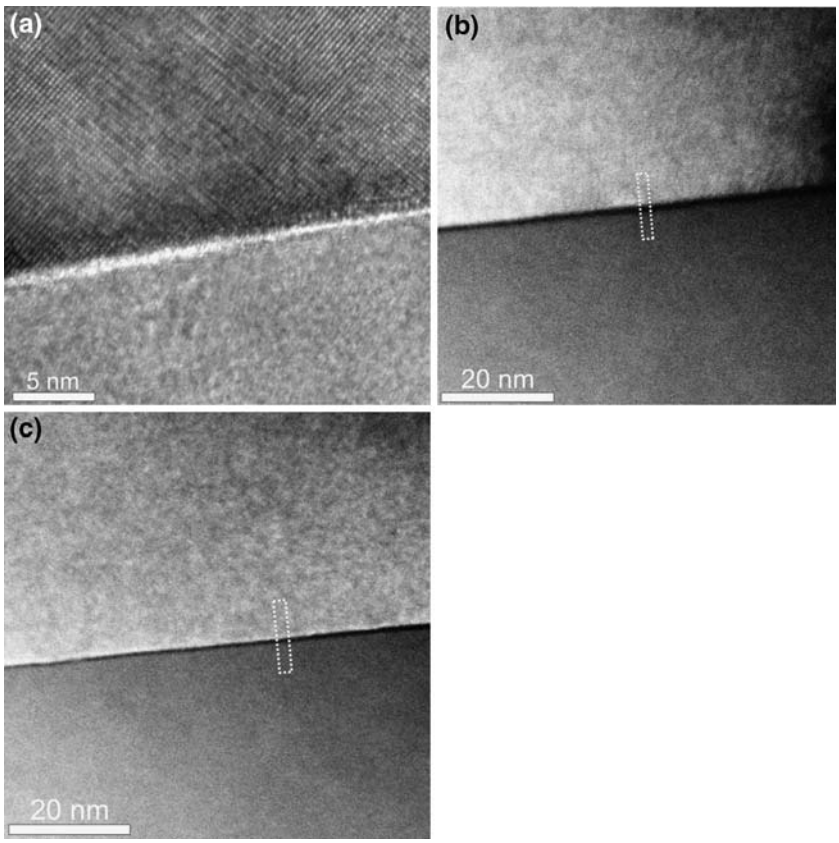

Fig. 5 A grain boundary in LSC with the upper grain oriented in the hexagonal [$\bar{4}\bar{2}1$] zone axis (equal to the cubic [001] zone axis). (**a**) A bright field TEM image, (**b**) a HAADF STEM image, and (**c**) a LAADF STEM image

EELS-SI was performed across three different grain boundaries and with both grains tilted away from Bragg conditions to avoid systematic errors in chemical composition due to channeling effects [24]. Representative EELS spectra from the SI with the peaks used in the quantitative analysis are shown in Fig. 7. The content of the different elements as a function of distance from the grain boundary is shown in Fig. 8. Over a distance of 6–8 nm the level of La and Sr decreases by about 5% compared to the bulk content and the relative amount of Co and O increases by the same amount. The width of the grain boundary layer is larger in Fig. 8 compared to the width of the low intensity layer in the ADF images in Fig. 5. The reason for this difference in width can be explained by the 3° tilt of the sample before EELS-SI was acquired. The grain boundary was therefore no longer edge on and the grain boundary layer was smeared out when averaged over the thickness of the TEM foil. The larger electron probe used in SI did also lower the spatial resolution compared to ADF imaging. Furthermore, drift due to the relatively long acquisition time of several minutes to record a complete spectrum image, might have lowered the spatial resolution of SI compared to ADF imaging, despite the use of drift compensation. The variations in chemical composition across the grain boundary layer compared to the bulk composition are therefore larger than indicated in Fig. 8. The changes in intensity across the grain boundary layer indicated in Fig. 6 may seem large compared to the relatively small changes in chemical composition indicated in Fig. 8. However, the Rutherford scattering is proportional to the $Z^{1.6–1.9}$ [29], and this strong Z dependence makes the ADF images extremely sensitive to variations in the heavy elements, like La and Sr. From the present analysis it is clear that a grain boundary layer, deficient on La and Sr, is present in LSC. The difference between the grain boundaries in LC and LSC will have consequences for the functional properties of the materials. In LSC, both the electronic and the ionic conductivity across the grain boundaries will be significantly influenced by the Co and O rich grain boundary layer. In addition, this grain boundary layer could also affect the mechanical properties, such as fracture strength and fracture toughness.

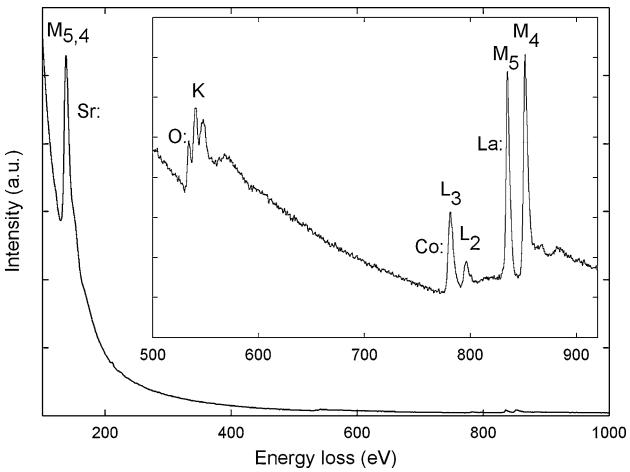

Fig. 7 EELS spectrum for LSC. The spectrum between 500 and 920 eV is shown in the inset

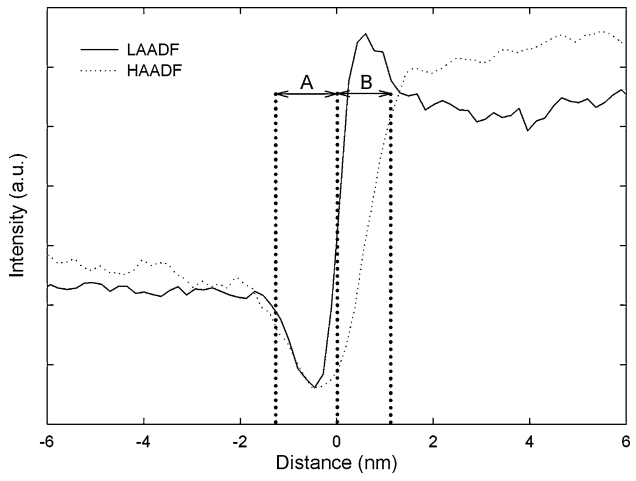

Fig. 6 The intensity profiles across the grain boundary for images (**b**) and (**c**) in Fig. 5. The grain boundary is located around 0 nm, with the out-of-zone grain below 0 nm and the in-zone grain above 0 nm. The profiles correspond to the rectangular dotted areas in Fig. 5(**b**) and (**c**). Region ''A'' is the low intensity layer and region ''B'' is the dechanneling layer

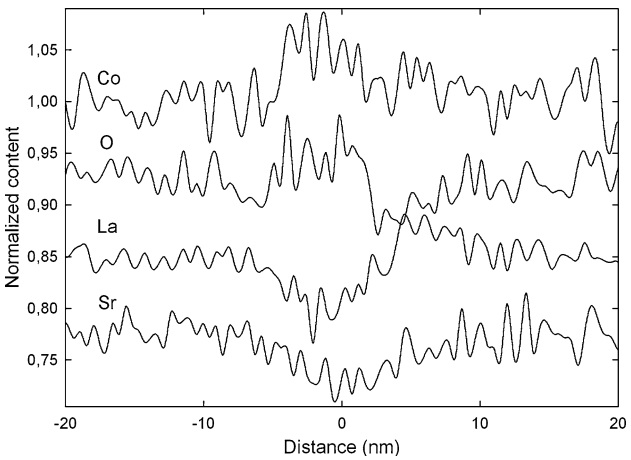

Fig. 8 The normalized content of the elements across the grain boundary in Fig. 5. The sample is tilted 3° compared to Fig. 5 to have both grains away from any zone axis. For clarity, the curves for O, La, and Sr are shifted by –0.075, –0.150, and –0.225, respectively, to distinguish the different elements

Conclusions

TEM has been used to study secondary phases and grain boundaries in $LaCoO_3$ and $La_{0.7}Sr_{0.3}CoO_{3-\delta}$. In both materials small amounts of Co_3O_4 with a cubic spinel structure were found at triple junctions. Grain boundaries were analysed using a combination of HRTEM, ADF imaging and EELS SI. Sharp boundaries with no traces of any secondary phases or variations in chemical composition were found in $LaCoO_3$. In $La_{0.7}Sr_{0.3}CoO_{3-\delta}$, however, 1–2 nm thick layers, rich in Co and O and deficient in La and Sr, were found at the grain boundaries.

Acknowledgements This work was supported by NTNU, strategic area of materials and The Research Council of Norway, grants no. 140553/420, 158517/431, and 153329/V30.

References

1. Dimos D, Chaudhari P, Mannhart J (1990) Phys Rev B 41:4038
2. Ivanov ZG, Nilsson PA, Winkler D, Alarco JA, Claeson T, Stepantsov EA, Tzalenchuk AY (1991) Appl Phys Lett 59:3030
3. Heinig NF, Redwing RD, Nordman JE, Larbalestier DC (1999) Phys Rev B 60:1409
4. Hammerl G, Schmehl A, Schulz RR, Goetz B, Bielefeldt H, Schneider CW, Hilgenkamp H, Mannhart J (2000) Nature 407:162
5. Kim YW, Mitomo M, Nishimura T (2002) J Am Ceram Soc. 85:1007
6. Kim YW, Mitomo M, Nishimura T (2001) J Am Ceram Soc. 84:2060
7. Cinibulk MK, Kleebe HJ, Schneider GA, Ruhle M (1993) J Am Ceram Soc. 76:2801
8. Tanaka I, Kleebe HJ, Cinibulk MK, Bruley J, Clarke DR, Ruhle M (1994) J Am Ceram Soc 77:911
9. Wang CM, Pan WQ, Hoffmann MJ, Cannon RM, Ruhle M (1996) J Am Ceram Soc 79:788
10. Mastin J, Einarsrud M-A, Grande T (2006) Chem Mater 18:1680
11. Thornton G, Tofield BC, Hewat AW (1986) J Solid State Chem 61:301
12. Mineshige A, Inaba M, Yao TS, Ogumi Z, Kikuchi K, Kawase M (1996) J Solid State Chem 121:423
13. Bouwmeester HJM, Gellings PJ (1997) The CRC handbook of solid state electrochemistry, CRC Press, Boca Raton
14. Williams DB, Carter CB (1996) Transmission electron microscopy. Plenum Press, New York
15. Pennycook SJ, Jesson DE (1991) Ultramicroscopy 37:14
16. Mitsuishi K, Takeguchi M, Yasuda H, Furuya K (2001) J Electron Microsc 50:157
17. Watanabe K, Yamazaki T, Hashimoto I, Shiojiri M (2001) Phys Rev B 64:115432
18. Klie RF, Zhu Y (2005) Micron 36:219
19. Morin F, Trudel G, Denos Y (1997) Solid State Ionics 96:129
20. Mastin J, Einarsrud M-A, Grande T (2006) Chem Mater 18:6047
21. Lide DR (1991) Handbook of chemistry and physics. CRC Press, Boca Raton
22. King RB (1994) Encyclopedia of inorganic chemistry. Wiley, Chichester
23. Lein HL, Andersen ØS, Vullum PE, Lara-Curzio E, Holmestad R, Einarsrud M-A, Grande T (2006) J Solid State Electrochem 10:635
24. Spence JCH, Taftø J (1983) J Micr 130:147
25. Perovic DD, Rossouw CJ, Howie A (1993) Utramicroscopy 52:353
26. Hillyard S, Silcox J (1995) Ultramicroscopy 58:6
27. Libera M, Ott JA, Siangchaew K (1996) Ultramicroscopy 63:81
28. Abe E, Pennycook SJ, Tsai AP (2003) Nature 421:347
29. Hartel P, Rose H, Dinges C (1996) Ultramicroscopy 63:93